Fabrication of sustainable hydrophobic and oleophilic pseudo-ordered macroporous Fe–Cu films with tunable composition and pore size via electrodeposition through colloidal templates

Evangelia Dislaki,[1,*] *Juho Pokki*[2], *Salvador Pané*[2], *Jordi Sort*[1,3], *Eva Pellicer*[1,*]

[1]Departament de Física, Universitat Autònoma de Barcelona, 08193 Bellaterra, Spain

[2]Institute of Robotics and Intelligent Systems, ETH Zurich, CH-8092, Zurich, Switzerland

[3]Institució Catalana de Recerca i Estudis Avançats (ICREA), Passeig Lluís Companys 23, 08010 Barcelona, Spain

E-mails: evangelia.dislaki@uab.cat

eva.pellicer@uab.cat

Keywords: electrodeposition; porous films; colloidal lithography; wettability; sustainability

Abstract

In this work, sustainable hydrophobic and oleophilic macroporous Fe–Cu films are fabricated using a straightforward, inexpensive and environmentally friendly two-step procedure which combines electrodeposition with the colloidal lithography technique. Elemental, morphological and structural characterization of the resulting pseudo-ordered meshes is carried out and wettability is assessed using contact angle measurements with respect to two distinct film compositions (3 at.% Fe vs 75-85 at.% Fe) and three different pore diameters (namely, 200 nm, 350 nm and 500 nm). Water contact angles are measured to be in the range of approximately 109.0°-155.1° (without any post-surface functionalization) and a low contact angle hysteresis is observed in the superhydrophobic samples. The increase in the hydrophobic character of the films correlates well with an increase in surface roughness, whereas differences in composition play a minor role. For the superhydrophobic Fe-rich macroporous film, water-oil separation capability and recyclability are also demonstrated while the pore size is favorable for effective water-oil mixture and emulsion separation. The results shown here demonstrate that sustainable and affordable materials processed in a simple and cheap pathway can be an asset for the removal of water-immiscible organic compounds from aqueous environments.

1. **Introduction**

Wetting phenomena observed in nature such as the water-repellent, non-adhesive surface of lotus leaves have attracted much attention due to the wide array of potential biomimetic technological applications in self-cleaning and anti-corrosion surfaces [1]. The anti-wetting behavior of lotus leaves is based on roughness promoted by micro- and nanoscale hierarchical surface characteristics along with the hydrophobic properties of the surface wax. In addition,

their non-sticky surface allows for the contaminants to be easily carried away by water droplets and, thus, involves a self-cleaning effect [2]. Furthermore, materials with switchable or antithetical wetting affinities, i.e. hydrophobic/oleophilic or hydrophilic/oleophobic can be utilized in oil-water separation applications such as tackling the environmental pollution caused by frequent oil spill accidents [3-5]. Methods that have been routinely employed in handling oil spill accidents such as booms and skimmers, dispersants, in situ burning and bioremediation are generally costly, inefficient and often result in secondary pollution which can be devastating to aquatic life as well as to other organisms [6-9]. Therefore, the development of inexpensive, sustainable and reusable materials that can separate the water and oil phases in an efficient way and even retrieve precious oil resources has garnered significant research attention in recent years. These materials function either through filtration (e.g. metallic meshes, textiles and membranes) or absorption (e.g. particles, sponges and aerogels) [3-5].

Fabrication of special wetting surfaces has been generally focused on tuning the surface morphology and composition in order to enhance the wetting properties and improve the separating efficiency. Functionalization of metallic meshes and textiles generally involves dip- or spray coating with polymers and optionally incorporating nanoparticles, hydrothermal reaction, in situ growth of micro- and nanocrystals or thermal oxidation to increase roughness followed by further modification by chemical treatment [3-5]. These materials are generally used in the separation of layered oil/water mixtures. In the case of emulsions, polymeric membranes have been proposed where by configuring the pore size to be smaller or commensurate with that of the emulsified droplets (typically < 20 μm), the water-oil emulsion can be separated since oil is allowed to pass through the pores and water is repelled [10]. However, the inherent difficulty of in-situ removal of oil from water in the filtration scheme, in addition to the issue of potential fouling or blockage with decreasing pore size which leads to a decline of permeation, has signalled towards absorption as a more promising strategy.

Highly porous materials are particularly targeted since the high surface-area-to-volume ratio leads to an increase of the capacity to absorb. Moreover, superhydrophobicity ensures water repellence, thereby enhancing oil absorption. Other desirable properties include eco-friendliness, reusability, recyclability, scalability and mechanical robustness. Nevertheless, many of the absorption materials currently described in literature can be difficult to handle, involve a complex preparation procedure, expensive precursors or specialized lab equipment (e.g. hydrothermal reaction, chemical vapor deposition, pyrolysis) and can also rely on subsequent treatment with toxic fluorinated compounds to reduce surface energy [3-5]. Several techniques exist for the preparation of porous metallic films such as dynamic template assisted electrodeposition [11], electron beam lithography [12] and colloidal templating [13]. Colloidal templating is a facile, cost-effective method of creating well-defined 3D porous structures by using 3D assembled colloids as a soft mask. Colloid size and assembly are critical factors that determine pore dimensions, wall and layer thickness and quality in terms of defect density. Various methods of crystallization techniques for monodisperse micro- and nanospheres such as vertical deposition [14], spin-coating [15], dip-coating [16], self-assembly [17], solvent evaporation [18], and electrophoretic deposition [19] have been reported in literature. Among these methods, electrophoretic deposition is an attractive option for achieving homogeneous coverage and assembly in a close-packed, oriented structure.

In this work, Fe–Cu porous coatings with hierarchical roughness and controllable pore dimensions were prepared using the colloidal templating technique coupled with electrodeposition from an environmentally-friendly electrolyte (Figure 1a,b). Fe–Cu is a particularly beneficial system as it consists of elements that are very affordable, abundant and nonhazardous. Additionally, electrodeposition was chosen for the growth of the films due to several advantages compared to other methods. Specifically, electrodeposition involves a simple, low-cost setup, it can be operated in ambient conditions without the requirement of

high vacuum and it enables the growth of relatively homogeneous coatings at fast rates. It also allows the creation of complex 3D geometries which are often unattainable by physical methods such as in the case of the patterned multi-layer porous architecture described in this work. The continuous Fe–Cu deposits were previously shown to exhibit a nodular, i.e. inherently rough morphology [20]. The added porous structure serves to further increase roughness and, therefore, the hydrophobic behavior of the coatings. Two distinct compositions and three sub-micron pore diameters were chosen in order to study the effects on water and oil contact angle (CA). High water CAs were achieved overall with one configuration exhibiting superhydrophobicity with an average water CA of 155.1° and a contact angle hysteresis (CHA) of 6.7°. The oleophilic behavior was also investigated revealing very low oil CA. Water-oil separation ability and reusability of the samples over multiple trials was demonstrated as a proof of concept (Figure 1c). Additionally, the small pore diameters are advantageous with respect to their potential towards separating both water-oil mixtures as well as emulsions while circumventing the fouling issues associated with membranes [21]. The entire fabrication process is upscalable and easy to implement in an industrial setting. Finally, the ferromagnetic properties of the Fe-rich Fe–Cu coatings [20] underscore the potential for magnetic manipulation and recyclability.

2. Materials and methods

2.1 Instrumentation

Electrophoretic deposition was implemented using a Keysight B2902A Precision Source / Measure Unit as a voltage source and a custom 3D-printed cell. The cell consisted of a 1 cm x 1 cm x 0.6 cm poly(methyl methacrylate) (PMMA) chamber glued to a platinized titanium sheet which served as a counter electrode. The substrate was fixed in place at a 0.5 cm distance from the counter electrode via indented slots at the back of the chamber.

Electrodeposition was carried out using a three-electrode cell connected to a Metrohm / Eco Chemie Autolab PGSTAT302N potentiostat / galvanostat. A Pt wire counter electrode and a double junction Ag|AgCl (E = +0.210V/SHE) reference electrode (Metrohm AG) with a 3M KCl inner solution and a 1M Na_2SO_4 outer solution were used. Silicon/silicon dioxide (Si/SiO_2) substrates with a 10 nm Ti adhesion layer and a 90 nm Au seed layer and cut into 1 x 1.5 cm dimensions were used. The working area was measured to be 1 ± 0.1 cm^2.

2.2 Colloidal suspension, Electrolyte Composition and Working Temperature

Monodisperse polystyrene (PS) sub-micron spheres in an 2.5% w/v solids aqueous suspension were purchased in three chosen dimensions (0.2, 0.35 and 0.5 μm) from Polysciences, Inc. to serve as templates. To prepare the solution for electrophoretic deposition, 0.05 ml of the PS sphere suspension was mixed in 0.45 ml of ethanol (0.25% w/v PS spheres in final solution). The electrolytes (100 ml) were prepared with Millipore Milli-Q water and ACS Reagent grade chemicals purchased from Sigma-Aldrich. The first solution contained 58.8 g/L $(NH_4)_2Fe(SO_4)_2 \cdot 6H_2O$, 1.25 g/L $CuSO_4 \cdot 5H_2O$, 7.9 g/L glycine as a complexing agent, 0.2 g/L sodium dodecyl sulfate as a wetting agent and 0.46 g/L saccharine as a grain refining agent. The pH was adjusted from 3.7 to 2.2 with addition of H_2SO_4 and samples were deposited at a temperature of 25 °C (bath A). For the second solution, glycine was substituted with 22.9 g/L of sodium gluconate as the complexing agent and samples were deposited from the as prepared solution with a pH of 4.1 at a temperature of 35 °C (bath B). The optimal electrolyte compositions and plating conditions were established in previous work [20].

2.3 Substrate Preparation and Fabrication Procedure

The substrates were initially cleaned with acetone, followed by isopropanol and, finally, rinsed with Milli-Q water to remove any debris and residues. As preparation for electrophoretic deposition they were treated with a 10 Mm solution of 3-mercapto-1-

propanesulfonic acid sodium salt (MPS, 90% purity from Sigma-Aldrich) in ethanol pre-heated to 50 °C for 1 h to increase the gold-coated substrate wettability [19]. Finally, they were alternatingly rinsed in Milli-Q water and ethanol to remove excessive MPS layers. After placing the substrate in the cell, the PS sphere solution was added, covering a 1cm^2 area [19]. A constant potential of 40 V cm^{-1} in the case of the two smaller sphere sizes and of 60 V cm^{-1} for the largest spheres was applied with deposition times of 1 min and 5 min, respectively [19]. Deposition time was tuned to allow for multi-layer assembly while preserving quality with regard to stability and number of defects. Following electrophoretic deposition, the samples were promptly placed on a hot plate and heated at 50 °C for 15 min [19]. Prior to performing electrodeposition, the Fe–Cu electrolyte was de-aerated with argon gas. Mild stirring during deposition was applied by means of a magnetic stirring bar (ω = 200 rpm). The galvanostatic mode was chosen with applied current densities of -10 mA cm^{-2} (Bath A) and -25 mA cm^{-2} (Bath B) and deposition times between 3-5 min (Bath A) and 15-50 seconds (Bath B) depending on desired thickness, namely targeting single or multi-layer coverage of the previously deposited spheres. Finally, the PS spheres were removed by immersing the samples in chloroform for 3 h followed by a final rinsing in acetone, ethanol and MQ-water.

2.4 Characterization

Sample morphology and roughness were observed using a Zeiss MERLIN Field Emission Scanning Electron Microscope (FE-SEM) and a MultiMode MMAFM-2 Atomic Force Microscope from Digital Instruments, Inc. The elemental composition was determined by Energy Dispersive X-ray Spectroscopy (EDXS) at an acceleration voltage of 15 kV. A Perkin Elmer Optima 4300DV Inductively Coupled Plasma Optical Emission Spectrometer (ICP-OES) was used to measure the mass of deposited Fe and Cu of two samples as part of an investigation into determining the potential loss of material when the samples are immersed in

an aqueous environment. In preparation, two samples were placed separately in beakers containing tap water for a duration of 120 hours then mildly rinsed with solvents, dried and dissolved in test tubes each containing 2 mL of nitric acid solution. One tube was filled solely with 2 mL nitric acid solution to be used as a reference and another with tap water reference. Finally, two test tubes were filled with 2 mL each of the tap water from the beakers where the samples were previously placed. The crystallographic structure of the deposits was studied by Grazing Incidence X-ray Diffraction (GIXRD) using CuK_{α} radiation and a Bragg-Brentano θ-2θ configuration with a grazing incidence angle of 1°. For further elemental analysis of the surface with a particular focus on the at.% of oxygen incorporated, X-ray Photoelectron Spectroscopy (XPS) analysis of several samples was carried out on a PHI 5500 Multitechnique System spectrometer from Physical Electronics, equipped with a monochromatic X-ray source placed perpendicular to the analyzer axis and calibrated using the 3d5/2 line of Ag. A contact angle analyzer (SmartDrop, Femtofab) was used to determine the water and oil contact angles at room temperature. The liquids used for the measurements were 3 μL droplets of ultrapure water and of motor oil, respectively. The reported values correspond to the average of three independent measurements at different sample locations.

2.5 Oil/water separation capability

The oil absorption capacity was assessed using Gas Chromatography–Mass Spectrometry (GC-MS) using commercially available motor oil (diesel mixture) and the analysis was based on the signal corresponding to diesel. Several droplets of oil with a volume ranging between 21-27 μL were placed with a micropipette in a beaker containing MQ water and a sample was manipulated using tweezers in order to approach the oil droplets where it could absorb and remove them from the water. The sample was then rinsed placed in a vial containing 5 mL of an internal standard (IS) solution, namely palmitic acid in hexane, immediately after the final iteration and the process was repeated for a second replica. The experiment was then

reiterated for 5 cycles of removal for 2 new replicas which were sonicated for 5 min in hexane and left to dry after each oil collection apart from the last round where they were placed in the vial with the IS solution. Finally, the same was done for 2 more replicas for a total of 10 cycles. All samples were then sonicated for 5 min to ensure complete oil separation from the samples and homogenization in the IS solution. To ensure that the samples were cleaned properly between iterations, 2 of the replicas were removed from the vials after sonication and placed in fresh vials with the IS solution and were once more sonicated for a 5 min duration.

3. Results and Discussion

3.1. Fabrication and characterization of porous films

The fabrication of the Fe–Cu porous films was conducted in two main steps. Firstly, the polystyrene (PS) sub-micron spheres were assembled onto the Au coated substrate in a close-packed structure via electrophoretic deposition based on the procedure established by Pokki *et al*. [22] A Scanning Electron Microscopy (SEM) micrograph of the self-assembled PS sphere layers can be seen in Figure 2. In the second step, based on our previous work [20] on the study and characterization of Fe–Cu continuous films, optimized electrolytes and plating conditions were chosen to deposit the Fe-rich and Cu-rich coatings in the interstices between the spheres. Upon removal of the spheres in the final step, the porous network was revealed with the pore sizes directly corresponding to the sphere diameters. This can be observed in the SEM micrographs in Figure 3a and 3b of the Cu-rich and Fe-rich films obtained, where plating time was calculated to cover multiple layers of spheres, thus resulting in a porous structure of two or more layers. Also, the pores are not randomly distributed but the occurrence of ordered or pseudo-ordered domains of ~1 μm^2 in size is apparent for some of the films.

Since wettability is a surface phenomenon, it was deemed necessary to further investigate the surface elemental composition of the films obtained. In Table 1, the at.% of Fe, Cu and O for all deposits, determined by X-ray photoelectron spectroscopy (XPS), are listed. It can be easily seen that the at.% of oxygen is consistently higher than 60 at.% indicating the presence of mainly Fe and Cu oxides at the surface which comes into contact with the water and oil droplets. Beneath this nanometer-thick passivation layer, the films are entirely metallic.

Table 1. Atomic percentage of Fe, Cu ad O at the uttermost film surface as determined via XPS. Notice that the correspondence between XPS (surface) and EDX (bulky) analyses is: 'Cu-rich' sample corresponds to 'Fe_3Cu_{97}' for the three pore sizes; 'Fe-rich' sample corresponds to '$Fe_{85}Cu_{15}$' for the 500 nm and 350 nm pore size, and to the '$Fe_{75}Cu_{25}$' for the 200 nm pore size.

	At.% at surface											
	Continuous			**500 nm**			**350 nm**			**200 nm**		
	Fe	**Cu**	**O**	**Fe**	**Cu**	**O**	**Fe**	**Cu**	**O**	**Fe**	**Cu**	**O**
Cu-rich	11.76	25.58	62.66	15.18	24.78	60.04	15.24	22.24	62.52	17.99	20.67	61.34
Fe-rich	25.64	10.89	63.46	16.12	16.98	66.91	14.57	12.17	73.26	15.89	14.94	69.17

Finally, for phase identification purposes, XRD analysis was performed on a number of Fe-rich samples. A representative diffractogram of a 350 nm pore size sample is shown in Figure 4. The Miller indices have also been included. Remarkably, in contrast to the Fe-rich continuous films with similar composition and a thickness of several microns which were found to be phase separated [20], the macroporous $Fe_{85}Cu_{15}$ films are shown to be single phase. This can be explained by the confined growth of the material at the sub-micron interstices between the PS spheres. It has been also observed for other systems like Cu-Ni that when the void size is sufficiently small, phase separation can be eventually suppressed [23]. Naturally, the oxide layer of a few nanometers found at the surface does not influence the XRD results as it is negligible compared to the overall interaction volume. The Cu-rich films

were expectedly single phase as the amount of Fe (3 at.%) is well below the solubility limit of the face-centered cubic (fcc)-Cu phase.

3.2. Water Wettability Assessment

The wetting behavior of the samples was assessed using the sessile drop method to determine the static CA. In general, all samples were found to be hydrophobic with CAs exceeding 134° for the Cu-rich and 145° for the Fe-rich porous coatings. In comparison, the Cu-rich and Fe-rich continuous films of similar composition electrodeposited under the same conditions as their porous counterparts had significantly lower water CA. Their morphology can be observed in the SEM micrographs in Figure 5.

In Table 2, the average value of the water CA for each sample can be viewed. Higher Fe content in the macroporous films was typically associated with an increase of roughness seen by the nano-size features along the pore walls and this is likely the reason for the enhanced hydrophobicity. Indeed, this is in agreement with previous studies showing that with an increase of roughness and even more so in the case of introducing hierarchical roughness, the hydrophobicity of the material is augmented [24-28]. Notably, the Fe-rich samples of 500 nm pore size were found to exhibit superhydrophobic behavior, as seen in Figure 6a, with water CAs consistently above 150° for all measurements. Importantly, the advancing and receding angles for the superhydrophobic sample were also measured and the calculated CAH of approximately 6.7° indicates a non-stick surface. Therefore, for the 500 nm sample transition to the Cassie-Baxter state [29,30], with air pocket formation underneath the droplet, is quite evident. Curiously, the CAH value of the Fe-rich sample of 350 nm pore diameter, seen in Figure 6b, was measured at a markedly higher value of 19.5°. For the latter case, it can be seen that there is at least partial wetting along the contact line. On the other hand, the hysteresis value for the continuous films was 10.7° for the Fe-rich and 17.3° for the Cu-rich,

respectively (see Figure S1a for the CA image of the continuous Fe-rich film). The Cu-rich continuous film is in a state closer to Wenzel as depicted in Figure 6c [31,32]. It is also worth mentioning that, in comparison, the most hydrophobic Cu-rich sample was that of 200 nm pore size with a relatively high average CA of 146° and a CAH of 16.6°. Nevertheless, the droplet appears pinned on the surface, as depicted in Figure 6d, indicating the presence of an intermediate state between the regimes of Wenzel and Cassie-Baxter with strong surface adhesion [33].

Table 2. Average water contact angles of Cu-rich and Fe-rich continuous and patterned films.

Composition	Water Contact Angle			
	Continuous	500 nm	350 nm	200 nm
Cu-rich	109.0°	136.2°	134.9°	146.0°
Fe-rich	135.8°	155.1°	145.24°	145.2°

At this point, it was essential to further study the topography and estimate the roughness of the Fe-rich macroporous samples that displayed higher CAs overall and to compare them to the continuous case. With this consideration, Atomic Force Microscopy (AFM) images were acquired for selected samples as seen in Figure 7. It can be seen that the porous morphology is quite well defined in the images. Moreover, the corresponding Root Mean Square (RMS) values of the height irregularities from an area of 5 μm x 5 μm were calculated at approximately 221.0 nm for the 500 nm pore sample, 140.5 nm for the 350 nm pore sample and 49.2 nm for the continuous film. This finding further supports the connection between increased roughness and higher CA. Finally, it is worth mentioning that the hydrophobic/superhydrophobic properties of the coatings are achieved without any post-surface functionalization of the electrodeposited layers, in contrast with other works dealing

with porous Fe-based alloy [34] or Cu films [35]. Even functionalized electrodeposited magnetite (Fe_3O_4) films exhibit much lower CA values [36].

3.3. Oleophilicity and Oil Droplet Collection Performance

Oil wettability was investigated for all samples using commercial car diesel oil as a model. A very oleophilic behavior with initial CAs between 13.0° and 18.9° and gradually decreasing was observed (see video V1 in the Supporting Information corresponding to a Cu-rich film of 200 nm pore diameter). A notable exception was the initial oil CA for Cu continuous films which was recorded at approximately 24.6°. The Fe continuous films also demonstrated the third highest oil CA of 18.8° which was very similar to that of the Cu-rich patterned films of 200 nm pore size measured at 18.9° (representative images of different samples during oil droplet placement are shown in Figures S1b, S1c and S1d of the Supporting Information). Next, the water/oil separation ability was assessed as a proof of concept using Fe-rich superhydrophobic samples due to their superior water repellent properties which would also allow for higher oil absorption. The samples were shown to have removed approximately 62% of the total oil added on average, as determined by gas chromatography–mass spectrometry analyses (see Materials and Methods section). Some losses were inevitably caused by the apparent tendency of the oil to adhere on the glass beaker which was used to hold the water/oil mixture and specifically along the contact line with the surface of the water. After 5 cycles of oil removal, a 45% of oil absorption was attained. Lastly, post 10 cycles the absorption seemed to hold at about 42%. Still images of a video recorded during a collection process can be seen in Figure 8 (see video V2 in the Supporting Information). In this case, the oil was mixed with graphite powder for improved contrast in the recording. Finally, the chemical stability of the films was tested by immersing them in tap water for 120 h and using Inductively Coupled Plasma Optical Emission Spectrometry (ICP-OES) measurements to

detect any material losses due to eventual corrosion. The result of these tests indicated that there was no Fe or Cu amount dissolved in the water after the 120-hour period when compared to the reference sample as can be verified in Table T1 of the Supporting Information.

4. Conclusion

Porous Fe–Cu coatings of Fe-rich (75-85 at.% Fe) and Cu-rich (3 at.% Fe) compositions and tunable pore size were prepared through a simple technique of combining electrodeposition and colloidal lithography.

Water/oil wettability measurements demonstrated the strongly hydrophobic/oleophilic nature of the deposits which was enhanced by the hierarchical roughness resulting from the patterned microstructure. Superhydrophobicity with a CA hysteresis of 6.7° was achieved for one configuration. Fe-rich deposits typically exhibited higher CAs than their Cu-rich counterparts, with one prominent exception, though this was also accompanied by a higher roughness observed in the pore walls of the former. This indicates that surface morphology may play a more significant role in the wetting characteristics of the coatings than elemental composition. Finally, an oil absorption capacity exceeding 60% on the first trial which is maintained at more than 40% after multiple removal cycles was documented.

Acknowledgements

This work was supported by the SELECTA (No. 642642) H2020-MSCA-ITN-2014 project**.** Partial financial support by the Spanish Government [Project MAT2017-86357- C3-1-R and associated FEDER], the Generalitat de Catalunya (2014-SGR-1015) and the European Research Council (SPIN-PORICS 2014-Consolidator Grant, Agreement nº 648454) is acknowledged. E.P. is grateful to MINECO for the "Ramon y Cajal" contract (RYC-2012-10839). J.P. acknowledges the contributions of Y. Çelik in the preparation of the 3D-printed setup for electrophoretic deposition, and P. Petit in 3D rendering of illustrations on porous films' fabrication. Authors acknowledge A. Eustaquio and O. Palacios from the Servei d'Anàlisi Química of Universitat Autònoma de Barcelona for the fruitful discussions on GC measurements.

Conflict of interest

All authors confirm that there is no conflict of interest.

Data availability statement

The raw/processed data required to reproduce these findings cannot be shared at this time due to technical or time limitations.

References

[1] B. Bhushan, Y. C. Jung, Prog. Mater. Sci. 56 (2011) 1.

[2] W. Barthlott, C. Neinhuis, Planta 202 (1997) 1.

[3] M. Qinglang, H. Cheng, A. G. Fane, R. Wang, H. Zhang, Small 12 (2016) 2186.

[4] B. Wang, W. Liang, Z. Guo, W. Liu, Chem. Soc. Rev. 44 (2015) 336.

[5] M. Ge, C. Cao, J. Huang, X. Zhang, Y. Tang, X. Zhou, K. Zhang, Z. Chen, Y. Lai, Nanoscale Horiz. 2018. Advance online publication. doi: 10.1039/C7NH00185A.

[6] D. A. E. G. Dave, A. E. Ghaly, Am. J. Environ. Sci. 7 (2011) 423.

[7] M. Fingas, The basics of oil spill cleanup. CRC press, Boca Raton, FL, USA 2012.

[8] S. Kleindienst, J. H. Paul, S. B. Joye, Nat. Rev. Microbiol. 13 (2015) 388.

[9] J. Fritt-Rasmussen, S. Wegeberg, K. Gustavson, Water Air Soil Pollut. 226 (2015) 329.

[10] W. Zhang, Z. Shi, F. Zhang, X. Liu, J. Jin, L. Jiang, Adv. Mater. 25 (2013) 2071.

[11] J. Zhang, M. D. Baró, E. Pellicer, J. Sort, Nanoscale 6 (2014) 12490.

[12] T.W Ebbesen, H.J. Lezec, H.F. Ghaemi, T. Thio, P.A. Wolff, Nature 391 (1998) 667.

[13] O.D. Velev, E.W. Kaler, Adv. Mater. 12 (2000) 531.

[14] P. Jiang, J. F. Bertone, K. S. Hwang, V. L. Colvin, Chem. Mater. 11 (1999) 2132.

[15] P. Jiang, T. Prasad, M. J. McFarland, V. L. Colvin, Appl. Phys. Lett. 89 (2006) 011908.

[16] Z. Z. Gu, A. Fujishima, O. Sato, Chem. Mater. 14 (2002) 760.

[17] Y. Yin, Y. Lu, B. Gates, Y. Xia, J. Am. Chem. Soc. 123 (2001) 8718.

[18] J.P. Hoogenboom, C. Retif, E. De Bres, M. Van De Boer, A. K. van Langen-Suurling, J. Romijn, A. Van Blaaderen, Nano Lett. 4 (2004) 205.

[19] A.L. Rogach, N. A. Kotov, D. S. Koktysh, J. W. Ostrander, G. A. Ragoisha, Chem. Mater. 12 (2000) 2721.

[20] E. Dislaki, J. Sort, E. Pellicer, Electrochim Acta 231 (2017) 739.

[21] Y. Peng, Z. Guo, J. Mater. Chem. A 4 (2016) 15749.

[22] J. Pokki, O. Ergeneman, K. M. Sivaraman, B. Özkale, M. A. Zeeshan, T. Lühmann, B. J. Nelson, S. Pane, Nanoscale 4 (2012) 3083.

[23] Z. Liu, G. Xia, F. Zhu, S. Kim, N. Markovic, C. L. Chien, and P. C. Searson, J. Appl. Phys. 103 (2008) 064313.

[24] M. Miwa, A. Nakajima, A. Fujishima, K. Hashimoto, T. Watanabe, Langmuir 16 (2000) 5754.

[25] L. Feng, S. Li, Y. Li, H. Li, L. Zhang, J. Zhai, Y. Song, B. Liu, L. Jiang, D. Zhu, Adv. Mater. 14 (2002) 1857.

[26] Z. Yoshimitsu, A. Nakajima, T. Watanabe, K. Hashimoto, Langmuir 18 (2002) 5818.

[27] D. Quéré, Physica A Stat. Mech. Appl. 313 (2002) 32.

[28] N.A. Patankar, Langmuir 20 (2004) 8209.

[29] A.B.D Cassie, J. Chem. Soc. Faraday Trans. 40 (1944) 546.

[30] S. Wang, L. Jiang, Adv. Mater. 19 (2007) 3423.

[31] R.N. Wenzel, Ind. Eng. Chem. 28 (1936) 988.

[32] D. Murakami, H. Jinnai, A. Takahara, Langmuir, 30 (2014) 2061.

[33] C.R. Szczepanski, F. Guittard, T. Darmanin, Adv. Colloid Interface Sci. 241 (2017) 37.

[34] S. Wang, Y. H. Ling, J. Zhang, J. J. Wang, G. Y. Xu, Int. J. Min. Metal. Mater. 21 (2014) 395.

[35] Y. Li, W. Z. Jia, Y. Y. Song, Y. H. Xia, Chem. Mater. 19 (2007) 5858.

[36] M. Cortés, E. Gómez, J. Sadler, E. Vallés, Electrochim. Acta 56 (2011) 4087.

Figure captions

Figure 1. Schematic representation of the work concept: a) PS spheres assembled on the substrate, b) electrodeposition of Fe-Cu followed by removal of the PS spheres, c) removal of oil from water using the hydrophobic and oleophilic macroporous Fe-Cu film.

Figure 2. PS spheres of 200 nm diameter assembled onto Au substrate via electrophoretic deposition.

Figure 3. Cu-rich porous films after removal of PS spheres of different diameters: a) Fe_3Cu_{97} porous films of 500 nm (top), 350 nm (middle) and 200 nm (bottom) pore diameters and b) $Fe_{85}Cu_{15}$ porous films of 500 nm (top) and 350 nm (middle) pore diameters and $Fe_{75}Cu_{25}$ film of 200 nm pore size (bottom).

Figure 4. XRD diffractogram obtained from a $Fe_{85}Cu_{15}$ (right) macroporous film.

Figure 5. SEM images of Fe_2Cu_{98} (left) and $Fe_{86}Cu_{15}$ (right) continuous film morphology.

Figure 6. Image taken during drop placement on the surface of: a) an Fe-rich superhydrophobic sample with 500 nm pores, b) an Fe-rich hydrophobic sample with 350 nm pores, c) a Cu-rich continuous hydrophobic sample, and d) a Cu-rich hydrophobic sample with 200 nm pores.

Figure 7. AFM images of a $Fe_{85}Cu_{15}$ macroporous film of (a) 350nm and (b) 500 nm pore size, and of (c) a continuous film of the same composition.

Figure 8. From a) to c) still images taken from a recording of the oil droplet removal process.

Graphical abstract

Hydrophobic, non-sticky, oleophilic, electroplated Fe–Cu coatings are patterned using colloidal lithography. This facile, cost-effective and environmental approach relies on hierarchical roughness to increase water-repellence and a highly porous morphology with sub-micrometre pore dimensions to boost oil absorption capacity. Deposits exhibit excellent substrate adhesion, good reusability and chemical stability when immersed in aqueous media.

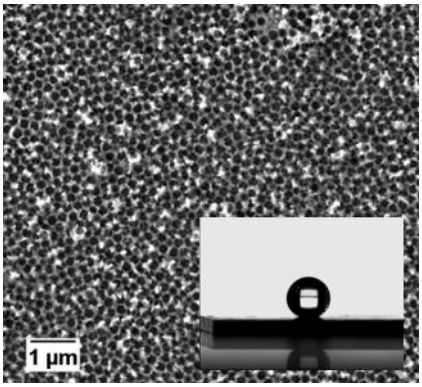

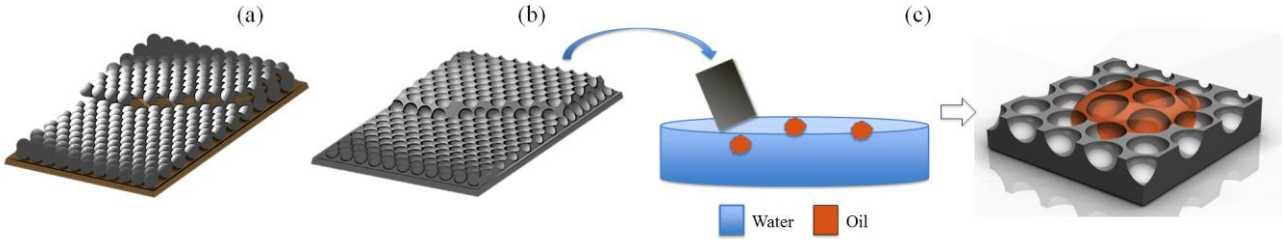

Figure 1

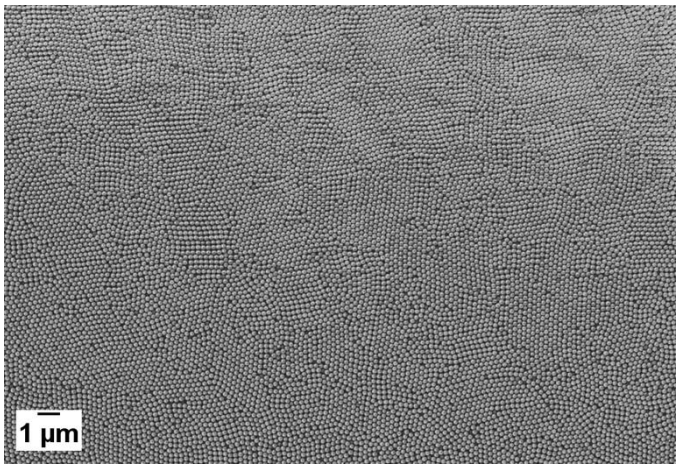

Figure 2

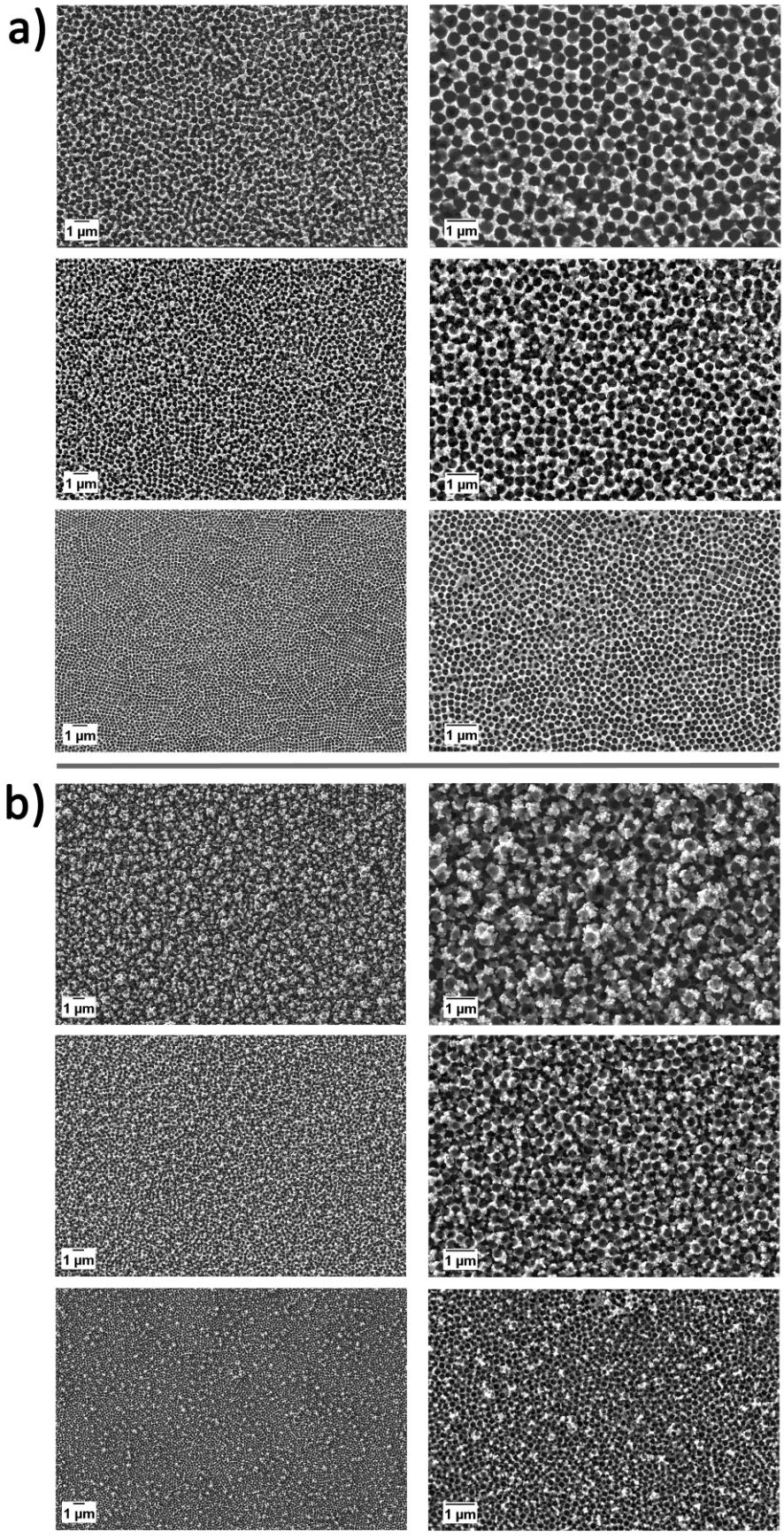

Figure 3

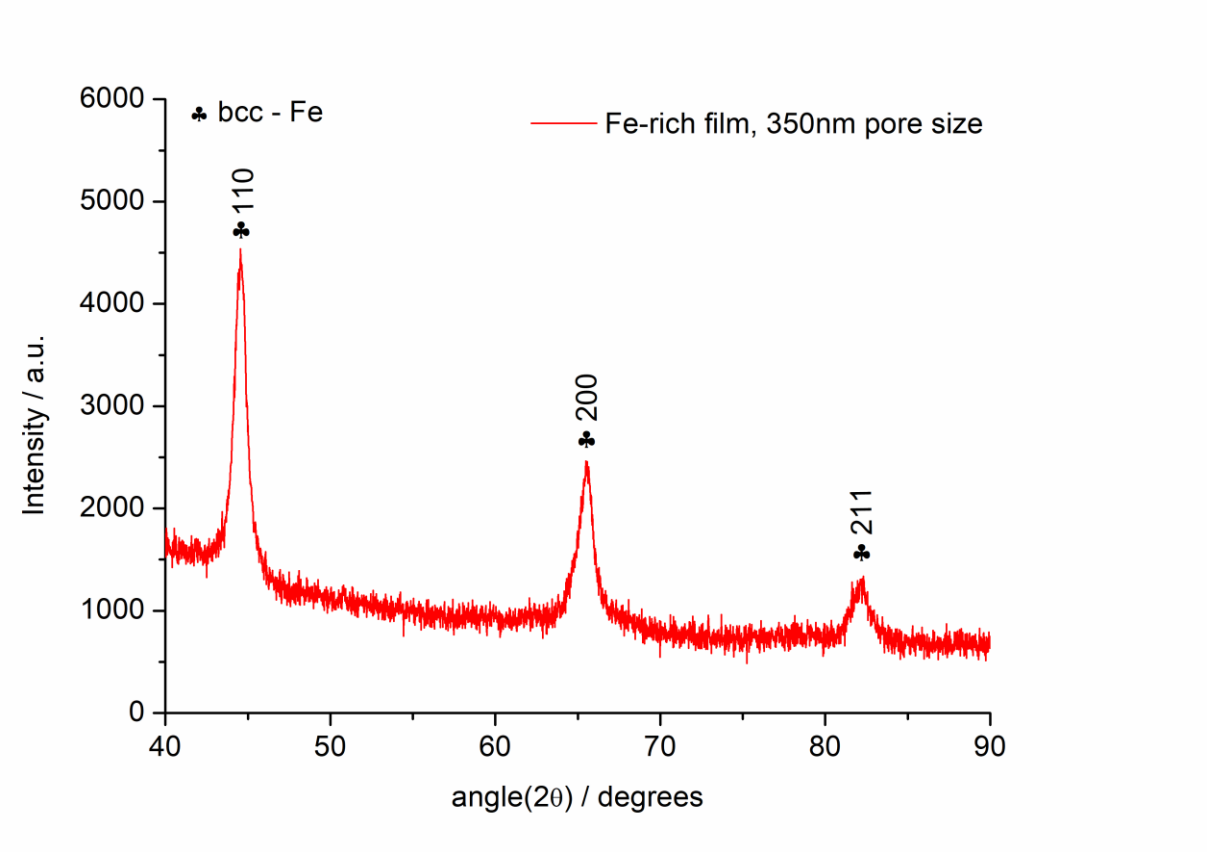
♣ bcc - Fe
Fe-rich film, 350nm pore size
♣ 110
♣ 200
♣ 211
Intensity / a.u.
angle(2θ) / degrees
0
1000
2000
3000
4000
5000
6000
40
50
60
70
80
90

Figure 4

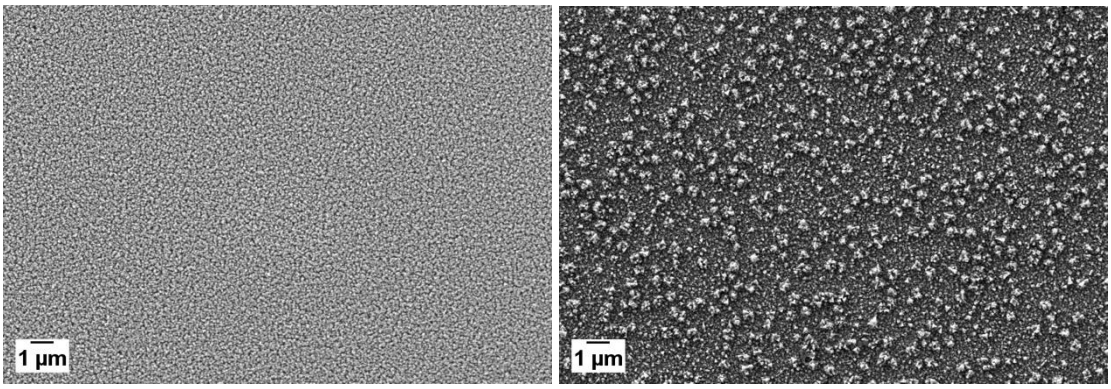

Figure 5

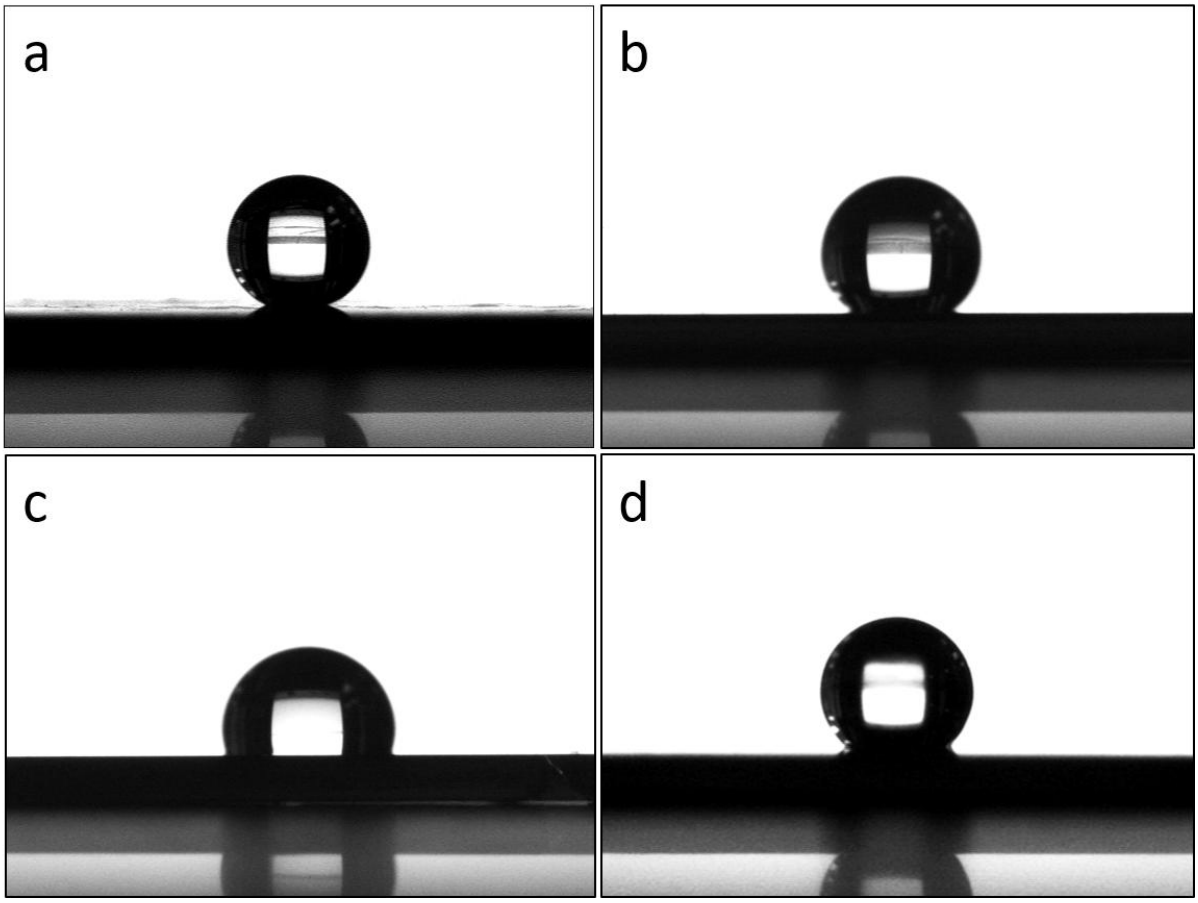

Figure 6

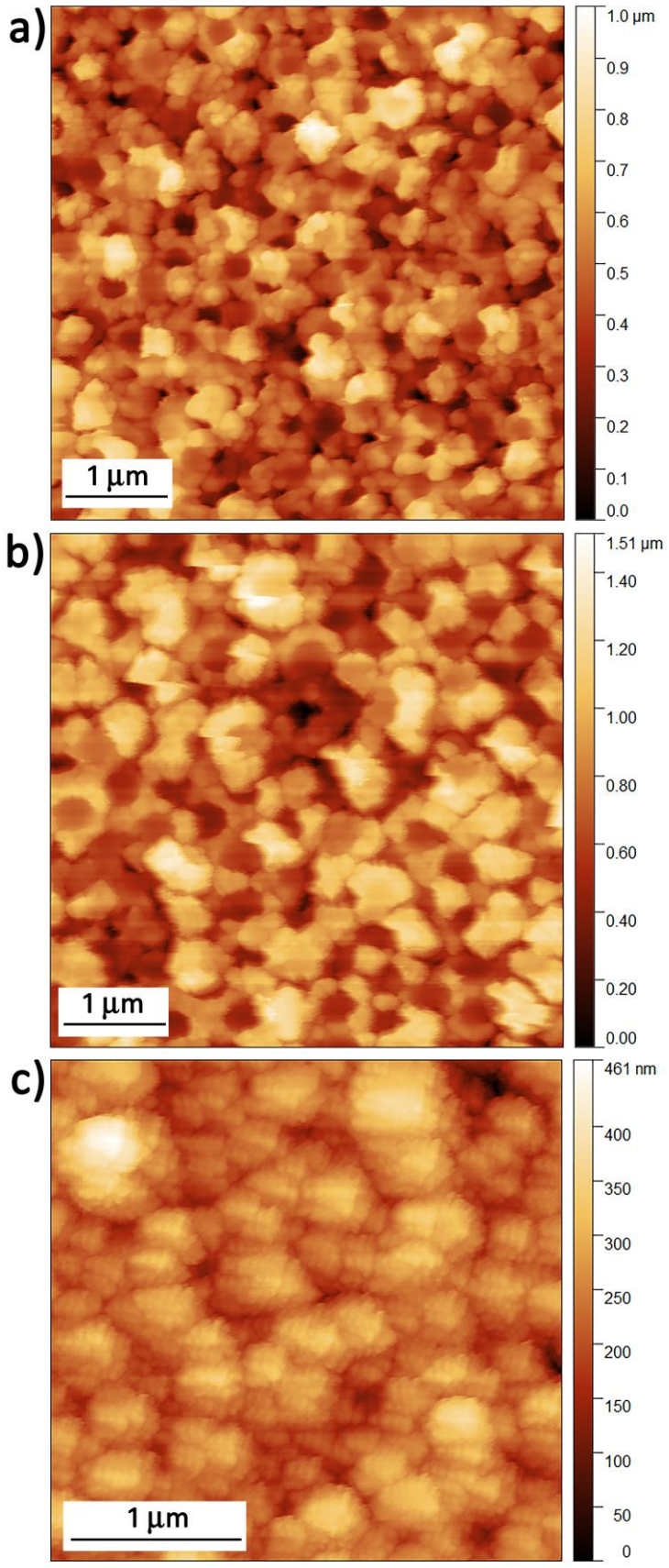
a)
1 µm
1.0 µm
0.9
0.8
0.7
0.6
0.5
0.4
0.3
0.2
0.1
0.0
b)
1 µm
1.51 µm
1.40
1.20
1.00
0.80
0.60
0.40
0.20
0.00
c)
1 µm
461 nm
400
350
300
250
200
150
100
50
0

Figure 7

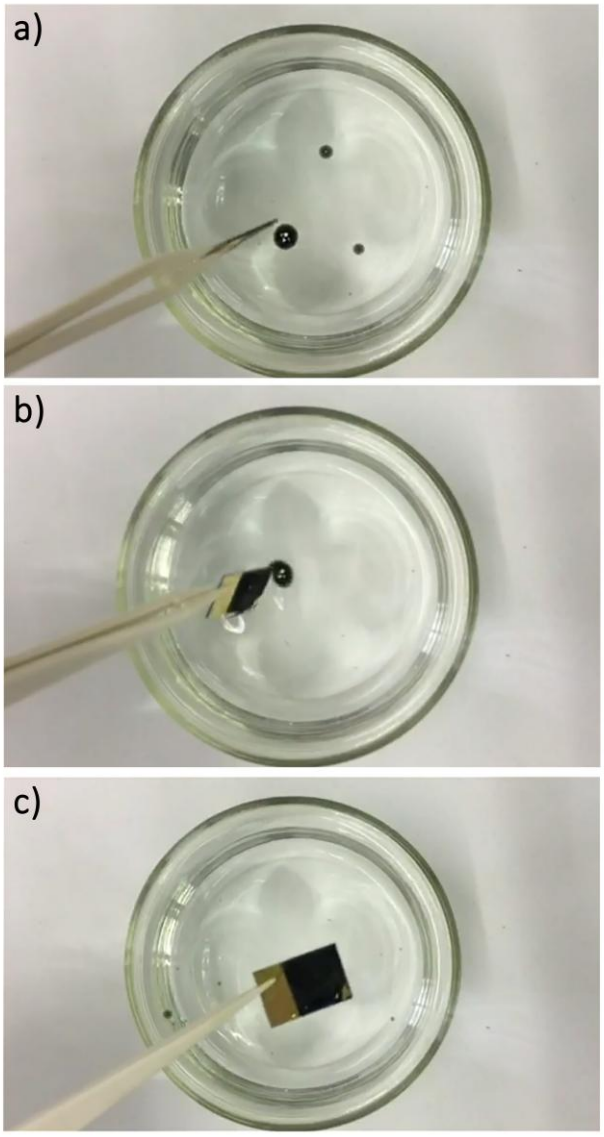

Figure 8